forum acusticum 2026
8-12 September · Graz, Austria

DATA-BASED DEFECT LOCALIZATION WITH LASER ULTRASOUND FOR SAMPLES WITH DOMINANT HIGHER-ORDER SCATTERING

Markus Saurer, Günther Paltauf, Robert Nuster

Department of Physics, University of Graz, Austria

Abstract

The advent of novel technologies capable of producing small samples with complex shapes, such as additive manufacturing and 3D printing, has given rise to new challenges for defect detection and visualization techniques, including laser ultrasonic imaging. When the ultrasonic wavelength is comparable to the sample dimensions, multiple reflections can dominate the wave field, resulting in severe artifacts in conventional physics-based reconstructions. In this study, a simplified numerical test case is used to compare a physics-based reconstruction approach with a data-driven convolutional neural network for defect localization in samples exhibiting dominant higher-order scattering. The results indicate that, within the investigated setup, the data-driven approach can identify defect locations in cases where strong multiple reflections limit the applicability of physics-based reconstructions. For the considered synthetic dataset, accuracies of up to 95 % were obtained on unseen test samples, and preliminary tests suggest that the trained model can generalize to selected cases outside the exact training grid. Overall, the study provides a first proof of concept that data-driven methods are a promising option for defect localization in laser-ultrasound scenarios dominated by higher-order scattering.

Keywords: *Laser Ultrasound, Defect Localization, Artificial Intelligence*

1. Introduction

Laser ultrasound (LUS) is an already established method for nondestructive testing. There are various use cases reported in literature where it is used to detect defects like air inclusions, cracks, and delaminations in different types of materials and sample shapes [1]. LUS utilizes a pulsed laser system to excite elastic waves via the photoacoustic effect and optically detects surface displacements caused by these elastic waves via interferometric or beam deflection methods. Besides the advantages of any ultrasound method being non-destructive and having high penetration depth and sensitivity, laser ultrasound adds the additional advantages of being a non-contact and broadband technique. Furthermore, it can be used in harsh environments, like for high-temperature applications. The fact that both excitation and detection are based on optical methods is advantageous for fast scanning and shaping of excitation/detection patterns.

Traditional ultrasound-based defect localization methods like the Synthetic Aperture Focusing Technique or the Total Focusing Method have been introduced to LUS by Stratoudaki et al. [2] and have been refined using the directivity and sensitivity distributions of laser-based ultrasound excitation and detection, respectively [3]. However, these traditional physics-based methods have certain limitations when being applied to samples with dominant higher-order scattered wavefields, like weld seams, as was shown previously in Saurer et al. [4]. Instead of seeking a reconstruction of the defect locations, a measure for the porosity was derived from the data. In Saurer et al. [5], a data-based method was used to obtain this measure for the porosity from samples without a distinct reference. In this work, data-based artificial intelligence (AI) methods will be used to localize defects in samples prone to a dominant higher-order scattered wavefield.

In general, AI methods have been used for classical ultrasound-based defect detection and characterization as well as for material characterization [6], [7]. Recent applications range from medical imaging [8] to crack sizing [9], elastic modulus distribution reconstruction [10], and porosity detection in carbon-fiber-reinforced-plastic components [11]. Additionally, there are also some recent advances using AI methods for LUS applications. Wang et al. [12] used it for the

Corresponding author: *ro.nuster@uni-graz.at.*

classification of seven different defects in aluminum samples, and Zhang et al. [13] analyzed Rayleigh waves to detect and classify surface and subsurface defects.

This work gives a first proof of concept that in samples with dominant higher-order scattering, data-based AI methods can be employed for defect localization. In the following, the numerical LUS scheme and the sample set will be briefly introduced. This is followed by the discussion of the problems of traditional reconstruction techniques. Subsequently, the data-based method will be described, and a first proof of concept will be shown. Finally, the advantages and disadvantages of the proposed method will be discussed.

2. Methods

For this study, a numerical scheme based on the Elastodynamic Finite Integration Technique implemented in Matlab was used. This method was introduced in Saurer et al. [4]. It solves the governing elastic equations on a staggered grid and additionally takes the optical and thermal phenomena into account that occur in the thermoelastic excitation regime.

The test case used in this study is illustrated in Fig. 1. As can be seen in the three-dimensional model of a representative sample in Fig. 1(a), rectangular-shaped aluminum samples with a cross-sectional area of 8 mm × 12 mm were used. Round, flat-bottom holes with a diameter of 2 mm were drilled into these samples, representing air inclusions. All the 15 possible positions for such air inclusions distributed over a grid of 3 × 5 are sketched in Fig. 1(b). This first investigation was restricted to scenarios with samples exhibiting a maximum of three inclusions, leading to a total of 576 different possibilities to distribute 0, 1, 2, or 3 defects on this grid. For 0 inclusions on this grid, there is 1 possibility, namely that nowhere is an air inclusion. For the distribution of one air inclusion, there are 15 possibilities, corresponding to the 15 different possible defect locations, and for distributing a total of 2 air inclusions, there are 105 different possibilities, and for 3 air inclusions, there are 455, making a total of 576 different inclusion scenarios. One representative of these possibilities is illustrated in Fig. 1(a), showing an air inclusion at the bottom left. The elongation of the samples in the third dimension (y-axis), in combination with time gating to filter out the echoes from these third-dimension interfaces, enables the use of a 2D numerical scheme as an approximation, thereby reducing the numerical effort.

For all the 576 possible inclusion scenarios, the two-dimensional elastic wave propagation was simulated numerically for 21 different excitation positions located between 2 and 10 mm away from the left edge on the upper surface of the sample. For each simulation, the surface displacement was stored at 88 different detection positions evenly distributed over the upper surface of the sample, resulting in a total of 88 B-scans for each sample. A B-scan in this work uses a fixed detection laser spot, and the distance d

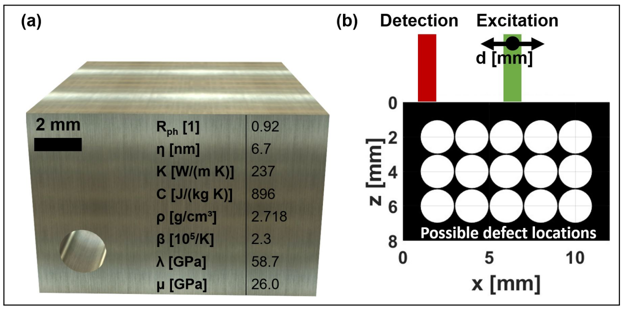

Figure 1: **(a)** Representative three-dimensional model of an aluminum sample used for testing AI-based defect location estimation. List of material parameters: R_{ph}...Reflectivity for 532 nm at normal incidence, η...Optical Penetration Depth, K...Thermal Conductivity, C...Heat Capacity, ρ...Density, β...Volumetric Thermal Expansion Coefficient, λ...1st Lamé Constant, μ...2nd Lamé Constant **(b)** Sketch showing all possible defect locations and the LUS measurement configuration. d....corresponds to the distance between the excitation and detection laser spot on the sample surface.

between the excitation and detection laser is varied by scanning the excitation laser over the surface, as indicated in Fig. 1(b). Each sample was divided into a grid of size 1333 × 889, and each pixel was either assigned the material parameters of aluminum listed in Fig. 1(a) or a medium that had the same acoustical impedance as air but a much higher speed of sound, which allows the use of a larger spatial step size. In general, to fulfill the discretization criteria, spatial and temporal discretization step sizes of 9 µm and 0.77 ns were utilized. The excitation laser had a Gaussian spatial and temporal profile with full width half maxima of 800 µm and 66 ns, respectively. The rather large excitation laser spot size was used to enhance the ratio of ultrasound bulk wave energy compared to ultrasound surface wave energy [1]. Furthermore, the ultrasound wavelength was thereby increased to become comparable to the sample dimensions in the x- and z-direction, which leads to a wavefield dominated by higher-order scattering, while also ensuring that the samples are easy to fabricate and handle. The simulation was stopped after 6 µs or 7812 timesteps, which is sufficient for all wave modes to travel around the sample but still keeps the computation time of the simulations within reasonable limits. In total, 12096 (576 × 21) simulations were conducted.

Two examples of such B-scans can be seen in Fig. 2. For these B-scans, the detection laser spot was placed near the edge of the sample, as depicted in Fig. 1(b). This spot on the edge was chosen to increase the influence of multi-reflections, since it is the aim of this work to investigate cases where multiple reflections are dominant. As can be seen, structures from surface waves (Rayleigh (R) and Surface Skimming Waves (SSW)), direct echoes from the air inclusions (longitudinal (LL) and transversal (TT)), mode-converted echoes (transversal to longitudinal (TL) and longitudinal to

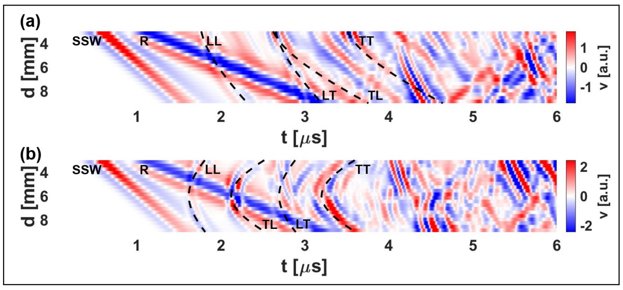

Figure 2: (a) B-scan for the sample illustrated in Fig. 1(a) using the detection position on the left edge, as depicted in Fig. 1(b). **(b)** B-scan for the sample with a defect in the center using the detection position on the left edge, as depicted in Fig. 1(b). The dotted lines indicate the theoretical arrival times of echoes from the inclusion (LL, TT, TL, LT), and the surface structures are labeled (SSW, R).

transversal (LT)), and high-intensity multi-reflections can be observed.

2.1. Physics-based Reconstruction

On top of the B-scans in Fig. 2, the theoretical arrival times $t^{th}_{i,j}$ of the direct and mode-converted echoes are plotted. Overall, they fit quite nicely with structures in the B-scan. The small deviations can be explained by the fact that for these calculations the approximation was used that the sound is scattered at the point of the inclusion that is closest to the upper surface. In general, the theoretical arrival times are calculated with the following equation:

$$t^{th}_{i,j} = \frac{\sqrt{(x^E_i - x^I)^2 + (z^E_i - z^I)^2}}{v_k} + \frac{\sqrt{(x^I - x^D_j)^2 + (z^I - z^D_j)^2}}{v_k} \tag{1}$$

which considers the knowledge of both excitation (x^E_i, z^E_i) and detection positions (x^D_j, z^D_j) as well as the inclusion position (x^I, z^I) and the speed of sound v_k for the different wave modes (v_L and v_T). The implemented physics-based reconstruction method utilizes this formula for the case that the inclusion position (x_I, z_I) is unknown. Each pixel of the reconstructed image is used as a potential defect location (x_I, z_I) and leads to a certain trajectory in the B-scan. The intensities along this trajectory are integrated and lead to the intensity value of this corresponding pixel in the reconstructed image. When there is an actual defect at the pixel, the trajectory overlaps quite nicely with the high-intensity structures in the B-scan (see Fig. 2), leading to a high intensity value at this pixel. This procedure can be done for various wave modes (LL, LT, TL, and TT) and different B-scans (detection positions). To omit any effects stemming from the surface waves, the signals of the reference sample without any inclusions were subtracted.

2.2. Data-based Defect Localization

The Convolution Neural Network (CNN) used for defect localization is sketched in Fig. 3. The normalized B-scan was first analyzed by a Conv2D layer, then a Flatten layer was used to convert the matrix into a vector, followed by a dropout layer with a rate of 0.1. The output layer was implemented as a dense layer of size (1, 15) with a sigmoid activation, thereby generating values between 0 and 1, corresponding to 15 predicted possibilities of an air inclusion at the respective lattice site, depicted in Fig. 1(b). For the training process, the Adam optimizer was used with a learning rate of 10^{-4} over 175 epochs, using a batch size of 3. To reduce the number of input pixels, the B-scans were down-sampled along the time direction to a time step of 77 ns, thereby neglecting frequencies above 6.5 MHz, resulting in a minimum wavelength of around 470 µm.

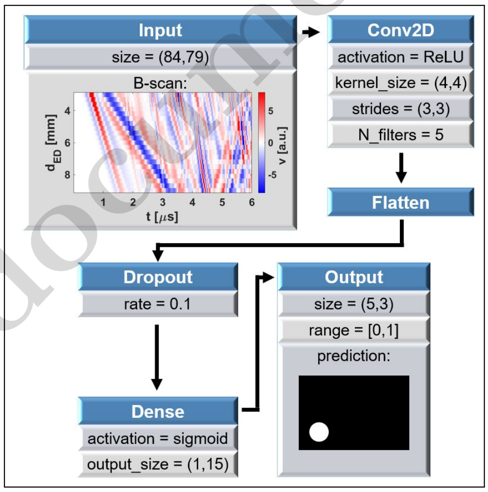

Figure 3: Neural network architecture together with a representative example of the input (normalized B-scan) and the output (probability of air inclusion at respective lattice site).

3. Results

3.1. Physics-based Reconstruction

In Fig. 4, the reconstructions of the sample with an inclusion in the center, using the second B-scan in Fig. 2, are shown. The different subplots (a-d) show the reconstructions using the various wave modes and subplot (e) the weighted sum of all images (normalized to the maximum of each image). In subplot (f), the sample composition is depicted with a red cross indicating the position of the detection. In all reconstructed images, artifacts of the other wave modes and of multiple reflections can be seen. However, except when using the LT mode, in all images there is a high-intensity structure at the top edge of the inclusion where the sound gets reflected. Which wave mode is useful depends on the location of the inclusion with respect to detection. Therefore, the weighted sum is used for all further investigations.

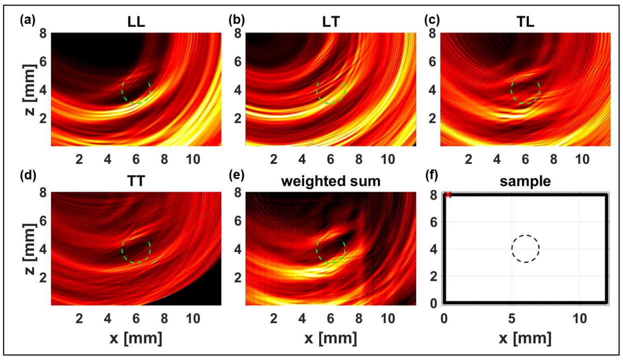

Figure 4: Physics-based reconstruction for the sample with an inclusion in the center (illustrated in **(f)**) for the different wave modes (**(a)** LL, **(b)** LT, **(c)** TL, and **(d)** TT) and the weighted sum of those in **(d)**.

To increase the quality of the reconstruction, the number of B-scans (number of detection points) can be increased. The reconstruction using two detection points in Fig. 5(a) has an improved image quality compared with Fig. 4(e). Using all 88 detection points leads to the image in Fig. 5(c), where the position of the inclusion is the most prominent structure and clearly visible. In Fig. 5(b and d), the reconstructed image for the sample with an inclusion at the bottom left is shown using 2 and 88 detection points, respectively. The reconstruction becomes worse due to the increased influence of the multiple reflections and because the inclusion is on the edge of the excitation and detection aperture. Nevertheless, the position of the inclusion can still be estimated.

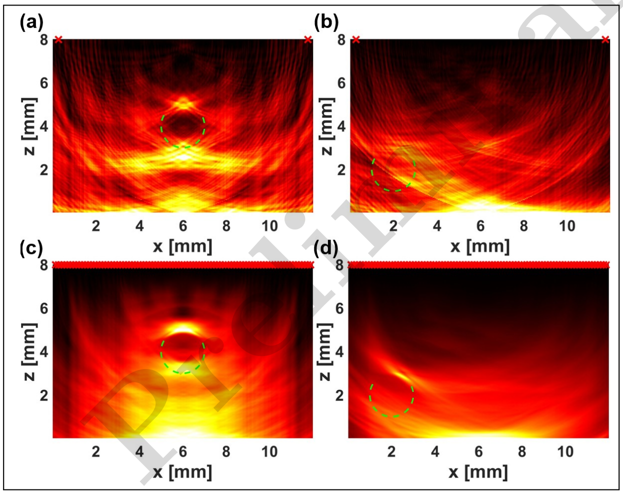

Figure 5: Physics-based reconstruction of the samples from Fig. 2, using two **(a-b)** and 88 **(c-d)** detection points, respectively.

Including more than one inclusion and thereby increasing the dominance of the higher-order scattering introduces further difficulties for the physics-based approach. In Fig. 6(a), the reconstruction for the case where both inclusions previously discussed are in the same sample can be seen. Due to shielding by the hole in the center, which remains visible, the inclusion in the lower left corner cannot be seen in the reconstruction. Similar effects can be seen in Fig. 6(b-d), where two or three inclusions are present. In all cases, not all inclusions can be localized in the reconstructed image, the others being masked by strong artifacts.

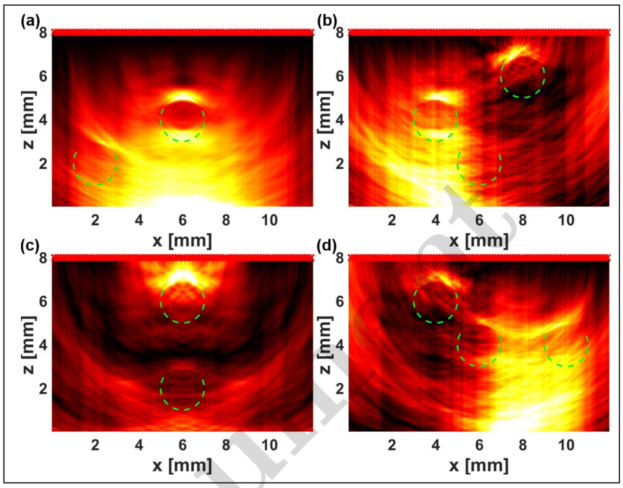

Figure 6: **(a-d)** Four representative examples of multiple reflections and shielding leading to difficulties for physics-based defect reconstruction.

These examples illustrate why a purely physics-based reconstruction becomes unreliable in the presence of strong multiple reflections and motivate the use of a data-driven approach in the following section. It has to be stated that there is literature available to enhance the physics-based reconstruction approach [14], [15], [16]. However, solving the reconstruction problem in the presence of dominant multiple reflections requires complex and cumbersome ray tracing, which becomes especially difficult when there is more than one defect existing. In that case, some kind of iterative approach, detecting one defect after another, would have to be applied.

3.2. Data-based Defect Localization

The dataset, comprising 576 samples, was randomly divided into two sets: 476 samples were allocated for training, while the remaining 100 samples were designated for testing. In a first step for each sample, only a single B-scan (detection position) is used. The performance of the trained model on the unseen B-scans from the four samples used for the physics-based reconstruction in Fig. 6(a-d) is displayed in Fig. 7. In the top row, the ground truth is plotted, and in the bottom row, the prediction of the CNN. The color corresponds to the true or predicted probability of an air inclusion p_{air} at the respective lattice site. As can be seen, the predictions are highly accurate, as most of the defect locations are correctly predicted.
For a more accurate evaluation of this model, it is necessary to account for two phenomena. First, the performance on the test set is dependent on the split-

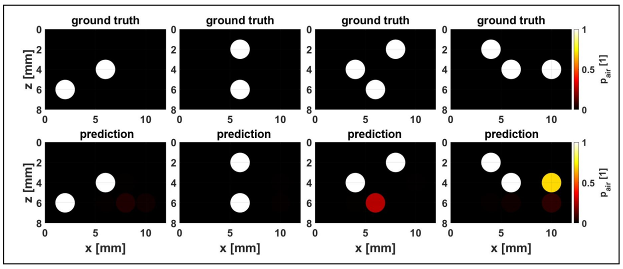

Figure 7: Data-based defect localization for the four samples from Fig. 6(a-d). In the first row the ground truths are plotted, and in the second row the predictions. p_{air} corresponds to the true and predicted probability of an air inclusion, respectively.

ting between training and test data. Consequently, the execution of statistical analyses over 70 different random splittings is imperative. Secondly, the performance of the model is dependent on the threshold that is used to divide the predictions of the model into inclusion and non-inclusion. This threshold can vary between 0 and 1, with 0.5 representing the most common choice. In Fig. 8, the results of the statistical analysis for various thresholds are plotted in red for this first case where just one B-scan (detection position) was used. As can be seen, the accuracy of the model on the unseen test data reaches a mean value of around 0.68 for correctly localizing all defects in a sample and, since in most falsely predicted samples the prediction of only one lattice site is wrong, 0.975 for correctly predicting the individual lattice sites. Due to the imbalanced nature of the training data set, which contains a significantly higher number of lattice sites without inclusion, the model tends towards lower values, resulting in the maxima being at a threshold of around 0.25.

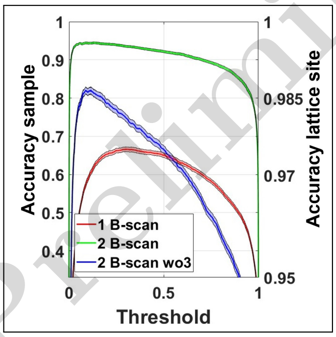

Figure 8: Threshold dependency of the mean accuracy of the neural network for correctly predicting the defect locations of the individual test samples (left axis) and the individual lattice sites (right axis) when using one B-scan (red), two B-scans (green), or two B-scans but a smaller dataset (blue).

Increasing the data by including a second detection position (B-scan), the accuracy can reach values of up to 0.95 and 0.995, respectively. On the other hand, reducing the number of samples to 121 (100 for training, 21 for testing) by neglecting the samples with 3 inclusions leads to a mean accuracy of 0.82 and 0.985, respectively. Thereby it can be concluded that the mean accuracy could still be enhanced by increasing the dataset (e.g., include all samples with 4 inclusions).

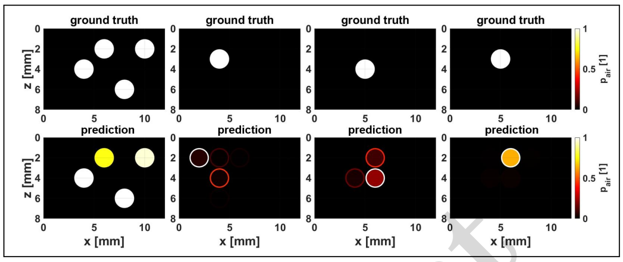

Figure 9: Four different tests of whether the neural network can interpolate to cases with four defects or to defects located between the grid of possible inclusion positions.

Since it was shown that the CNN can be used for defect localization in samples with dominant higher-order scattering, as a further step, its ability to interpolate to cases that have not been included in the training dataset was tested. The results of these investigations are depicted in Fig. 9. In the first image it can be seen that the CNN can successfully interpolate to a sample with four defects. The other three images show cases where the sample was placed in between individual lattice sites. In the second image, the inclusion was displaced in the vertical direction; in the third image, in the horizontal direction; and in the fourth image, in both the horizontal and vertical directions. Since the model has not been optimized for this interpolation, the probability at all lattice sites is rather low (face color at lattice site). However, after normalization (ring color at lattice site), it can be observed that lattice sites closest to the actual position of the inclusion have the highest probabilities. These first tests demonstrate the ability of the CNN to interpolate between the grid points used for training.

4. Summary and Conclusions

Overall, this simplified example of an object with a two-dimensional geometry containing air inclusions of equal size and shape demonstrates the potential of a CNN for defect localization in samples prone to a higher-order scattered wave field. In addition, the capability of interpolating to scenarios not included in the data set has been demonstrated, using a different number of defects and defects not located on the training grid. A notable advantage of the data-based approach is the transfer of most of the computational effort to a time before the actual application. Consequently, once the network is trained, it can perform real-time analyses. An additional advantage for possible applications is that the output of the data-based approach is a probability and thereby easier to interpret compared with the physics-based reconstructed image. Moreover, it was found that the data-based approach led to satisfactory results using just two B-scans (detection positions). However, the drawback compared to the physics-based approach remains the need for a large data set that reflects the possible varieties in sample and defect geometry. Additionally, when making predictions on experimental data, the model must be trained on data that closely reflect the experimental conditions, including noise. For future localizations of more complex structures, the grid displayed in Fig. 1(b) would have to be made much finer, which in turn would dramatically increase the number of possible defects and thus also the computational effort. As an alternative, the physics-based reconstruction images can be used as an input for the data-based approach.

5. Acknowledgments

This work was part of the IMPROFE project (no.: 883940) funded by the Austrian Research Promotion Agency (FFG).

References

[1] M. Saurer, G. Paltauf, and R. Nuster, "Laser ultrasound wave pattern analysis for efficient defect detection in samples with curved surfaces," *Photoacoustics*, vol. 40, p. 100 654, 2024. DOI: 10.1016/j.pacs.2024.100654.

[2] T. Stratoudaki, M. Clark, and P. D. Wilcox, "Laser induced ultrasonic phased array using full matrix capture data acquisition and total focusing method," *Optics express*, vol. 24, no. 19, pp. 21 921–21 938, 2016. DOI: 10.1364/OE.24.021921.

[3] R. Fuentes-Domínguez, M. Todd, T. Stratoudaki, R. J. Smith, and M. Clark, "Adaptive laser-induced phased arrays for imaging of defects on arbitrary non-flat surfaces," *NDT & E International*, vol. 161, p. 103 723, 2026, ISSN: 0963-8695. DOI: 10.1016/j.ndteint.2026.103723.

[4] M. Saurer, G. Paltauf, and R. Nuster, "Efficient testing of weld seam models with radii of curvature in the millimeter range using laser ultrasound," *Ultrasonics*, vol. 139, p. 107 292, 2024. DOI: 10.1016/j.ultras.2024.107292.

[5] M. Saurer et al., "Artificial intelligence-assisted laser ultrasound method for the estimation of porosity in hairpin weld seams," *Photoacoustics*, p. 100 770, 2025. DOI: 10.1016/j.pacs.2025.100770.

[6] S. Cantero-Chinchilla, P. D. Wilcox, and A. J. Croxford, "Deep learning in automated ultrasonic nde – developments, axioms and opportunities," *NDT & E International*, vol. 131, p. 102 703, 2022, ISSN: 0963-8695. DOI: 10.1016/j.ndteint.2022.102703.

[7] B. I, K. Barashok, Y. Choi, Y. Choi, M. Aslam, and J. Lee, "Machine learning techniques in ultrasonics-based defect detection and material characterization: A comprehensive review," *Advances in Mechanical Engineering*, vol. 17, no. 6, p. 16 878 132 251 347 390, 2025. DOI: 10.1177/16878132251347390.

[8] H. Wang et al., *Openpros: A large-scale dataset for limited view prostate ultrasound computed tomography*, 2025. DOI: 10.48550/arXiv.2505.12261.

[9] Q. Fei et al., "A deep learning-based ultrasonic diffraction data analysis method for accurate automatic crack sizing," *Applied Sciences*, vol. 14, p. 4619, May 2024. DOI: 10.3390/app14114619.

[10] U. R. Tuladhar, R. A. Simon, C. A. Linte, and M. S. Richards, "Ultrasound elastic modulus reconstruction using a deep learning model trained with simulated data," *Journal of Medical Imaging*, vol. 12, no. 1, pp. 017 001–017 001, 2025. DOI: 10.1117/1.JMI.12.1.017001.

[11] M. M. Vasilache, R. B. Tayong, and V. Velisavljevic, "Comprehensive review on the use of machine learning techniques applied to the ultrasound data for the characterisation of porosity across carbon fibre reinforced polymer layers," *Applied Composite Materials*, pp. 1–25, 2025. DOI: 10.1007/s10443-025-10342-4.

[12] S. Wang et al., "Internal defect detection model based on laser ultrasonic signal decomposition and deep learning," *Measurement*, vol. 242, p. 116 194, 2025, ISSN: 0263-2241. DOI: 10.1016/j.measurement.2024.116194.

[13] J. Zhang et al., "Laser ultrasonic inspection of surface and subsurface defects in materials based on deep learning," *Nondestructive Testing and Evaluation*, vol. 40, no. 10, pp. 4744–4763, 2025. DOI: 10.1080/10589759.2024.2429691.

[14] H. He, K. Sun, C. Sun, J. He, E. Liang, and Q. Liu, "Suppressing artifacts in the total focusing method using the directivity of laser ultrasound," *Photoacoustics*, vol. 31, p. 100 490, 2023, ISSN: 2213-5979. DOI: 10.1016/j.pacs.2023.100490.

[15] P. Lukacs, T. Stratoudaki, G. Davis, and T. Gachagan, "Online evolution of a phased array for ultrasonic imaging by a novel adaptive data acquisition method," *Scientific Reports*, vol. 14, Apr. 2024. DOI: 10.1038/s41598-024-59099-z.

[16] P. Wang et al., "Optimization of total focusing sparse array imaging based on the zero-crossing factor," *Measurement*, vol. 256, p. 118 428, 2025, ISSN: 0263-2241. DOI: 10.1016/j.measurement.2025.118428.